Comparison between Wall-modeled and Wall-resolved Large Eddy Simulations for the prediction of boundary-layer separation around the side mirror of a full-scale vehicle

Kei Ambo[*], Takashi Yoshino[†], Tesuhiro Kawamura[‡], Minoru Teramura[§],
Honda R&D Co., Ltd., Haga-gun, Tochigi, 321-3393, Japan

David A. Philips[¶], Guillaume A. Brès[**] and Sanjeeb T. Bose[††]
Cascade Technologies Inc., Palo Alto, California 94303, USA

Aeroacoustic noise is generated by boundary layer separation around side-mirrors of a vehicle. Since this type of flow includes transition phenomenon, CFD sensitivity is influenced by the several factors including wall modeling, solver formulation, solver scheme and mesh resolution. In order to predict boundary layer separation and vortex shedding around a side mirror, a high-fidelity Large Eddy Simulation (LES) methodology developed by Cascade Technologies was applied. In particular, dynamic slip wall modeling and Voronoi diagram based meshing were unique features of the approach. In this paper, the effectiveness was investigated by comparing the experimental pressure coefficient (Cp) data and wall resolved LES with the wall modeled LES. As the results, it was confirmed that this unique code could predict the boundary layer separation at a super-critical Reynolds number. A grid point was not required in the viscous bottom layer leading to a minimum normalized wall distance y+ of final case of approximately 7.0. It is shown that the wall normal resolution can be set 8 times larger than that of the wall resolved LES. Therefore the cell reduction directly influences the total calculation cost in the prediction of the boundary layer separation for the industrial use.

Nomenclature

Re	=	Reynolds number
$y+$	=	Normalized wall normal distance
p	=	Pressure
C_p	=	Pressure coefficient
ρ	=	Density
s	=	Entropy
c	=	Speed of sound
Δt	=	Time step
σ_{ij}	=	Viscous stress
u	=	Fluid velocity
x, y, z	=	Cartesian coordinates

[*] Assistant Chief Engineer, kei_ambo@n.t.rd.honda.co.jp
[†] Assistant Chief Engineer
[‡] Assistant Chief Engineer
[§] Chief Engineer
[¶] Research Scientist
[**] Senior Research Scientist
[††] Chief Technology Officer

I. Introduction

Modern automotive design practices strive to increase passenger comfort through interior noise reduction, in addition to the improvement of increased fuel efficiency. Sound sources[1] for vehicle interior noise include noise from the engine, exhaust, and drive power transmission; road noise from the tires and vibrations of the suspension; noise from heating, ventilation, and air conditioning (HVAC) systems; and flow-induced noise generated by air flow separation around each part of the vehicle[2,3]. In that latter category, high-frequency aeroacoustic noise (over 1 kHz) generated around side-mirrors and transmitted into the passenger cabin via the window glass (Ambo et al.[4]) is considered particularly important. As alternative power plant approaches (Hybrids, EVs) have reduced engine and transmission noise, flow induced noise has become a larger and more noticeable component of the total interior noise.

The present work examines the challenges of modeling the source of this noise, i.e., the pressure fluctuations from boundary layer separation and vortex shedding around the side mirror. Emphasis is given to the development of a high-fidelity Large-Eddy Simulation (LES) methodology that accurately captures the relevant physics at a cost that supports industrial use. Wind-tunnel measurements and LES of the flow around a 2010M Honda FIT (width 1695mm, length 3900mm, height 1550mm) are presented, with comparisons between the experimental data and numerical predictions focusing on the side mirror surface pressure.

A key element of the LES methodology is the use of the dynamic slip wall model (DSWM) of Bose and Moin[5]. Wall resolved LES (WRLES) suffers from a near quadratic increase in the number of grid points with respect to the Reynolds number ($N \sim Re^{13/7}$) as compared with a linear scaling for wall modeled LES (WMLES)[6]. Data presented from WRLES computations performed on a 5.5-Billion cell mesh using the unstructured finite volume method (FVM) code[7,8] running on Japan's "K-Computer" illustrates the high cost of WRLES but also the ability to capture transition and separation physics. Predicting these complex phenomena has been challenging for traditional wall-modeling approaches that rely on assumptions about local flow conditions (e.g. turbulent flow, profile shape, equilibrium conditions). In contrast, the DSWM derives the wall boundary condition directly from the filtered LES governing equations. While this is an important step, it is not in itself sufficient to guarantee success in capturing complex flow phenomena at a tractable computational cost. Therefore, WMLES computations, performed by Cascade Technologies' CharLES code, explore the sensitivities of several factors including wall modeling, a low-dissipation solver formulation, a novel time advancement scheme, and targeted mesh refinement.

II. Challenges Predicting Mirror Flow Separation

A. Full Vehicle Experiments

The experimental measurements were conducted in a closed loop wind tunnel owned by Honda named "HAGA WT" for a full-scale vehicle[9]. Figure 1. shows the pressure tap locations in the mirror made using stereo lithography. The A-plane is the horizontal section of the mirror, and the B-plane is the vertical section. The pressure coefficient (Cp) distribution on the mirror surface was measured. These pressure taps were connected to ZOC33 (64ch, Scanivalve corporation). The sampling time was 6.4×10^{-3} seconds, and the measurement time was 64 seconds. Cp distribution of a velocity sweep from 80km/h to 100km/h is shown in Figure 2. The corresponding Reynolds number is change is approximately 2.27×10^{5} to 2.84×10^{5} based on the mirror height. As the velocity (and therefore Reynolds number) is increased, it is evident that the side-mirror of vehicle experiences flow transition at probe point 9 to 14 and 21 to 27

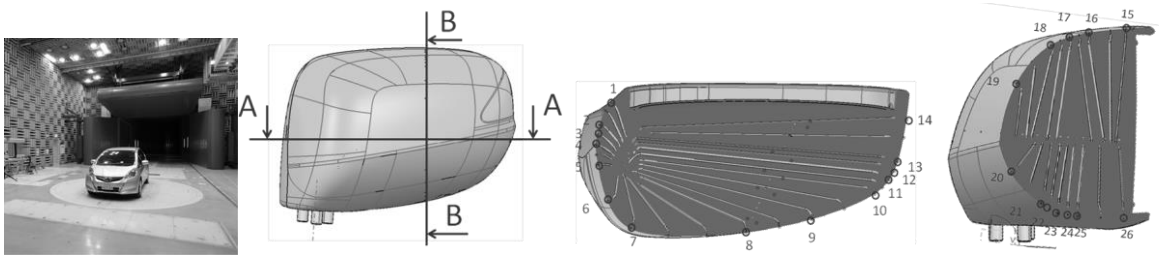

(a) wind tunnel (b) Section of mirror (c) A-plane (d) B-plane

Figure 1. Probe position of measurement. *Probe number of A-plane is 1 to 14, and B-plane is 15 to 26.*

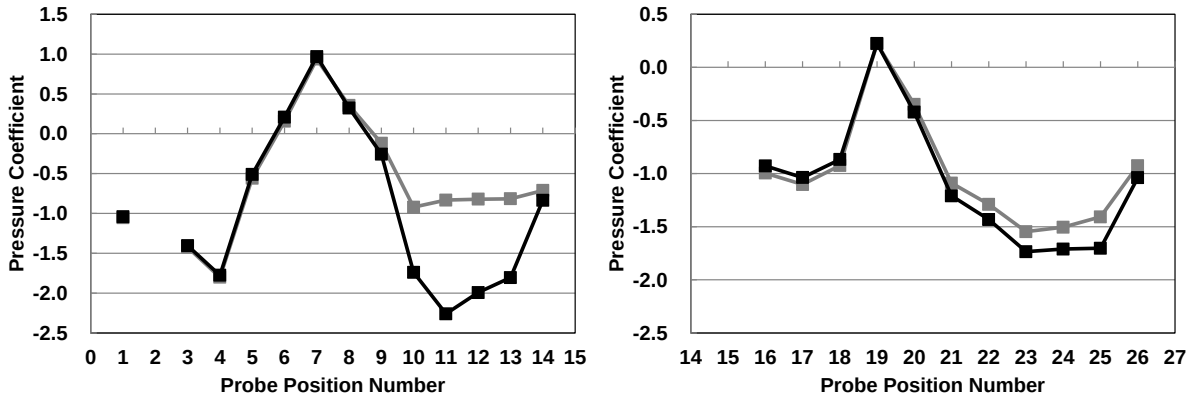

(a) A-plane (b) B-plane

Figure 2. Pressure coefficient. *Cp at probe position, A-plane (left) and B-plane (right):80km/h* ( ), *100km/h* ( ).

B. Wall-Resolved Simulations

Wall-Resolved LES was performed using the unstructured FVM code[7,8] at the conditions described in Table 1. Additionally, the tire and ground are in a stationary state to match the wind tunnel conditions. A slip ground boundary condition is used for x<-7.75m and a no-slip condition is used for x≥-7.75m. This computation used a Spalding wall law[10] which including linear and log-law distribution depending on the normal wall distance from the boundary surface. The side mirror boundary layers were fully resolved, but the remainder of the vehicle used a log-law approximation. The mesh resolution required to captured the Cp distribution in this simulation around side-mirror was approximately 0.2mm(wall horizontal direction) and 0.015mm(wall normal direction). In addition, the surface mesh resolution around body is approximately 1.0mm(wall horizontal direction). The resulting element count is 5.5 billion cells including unstructured tetra and prism cell. Cp data from a initial simulation is presented next.

Discretization method	Unstructured FVM
Vehicle/ mirror length [mm]	3,900mm / 149.1mm
Velocity [m/s]	27.7 (100km/h)
Reynolds number based on mirror	2.84×10^5
SGS turbulence model	Smagorinsky-Lilly (Cs=0.15)
Time marching method	1st order Euler
Spatial discretization	2nd order CD (5% 1st upwind is blended in convection terms)
P-V coupling method	SMAC method
Boundary conditions	FIT body:spalding wall law Ground: Slip & spalding wall law

Table 1. Simulation conditions. *wall resolved large eddy simulation case.*

The Cp distribution provided by experiment and by LES are compared in Figure 3. The vertical axis shows Cp, and the horizontal axis shows the numbered pressure taps. The results of the wall resolved simulation accurately predicts the Cp distribution.

It is evident that a very fine mesh was required in the wall-resolved LES to predict the boundary layer separation around the critical Reynolds number. To accurately capture the relevant flow physics at more tractable computational costs, the use of the wall modeling in large eddy simulations is therefore explored in the next sections.

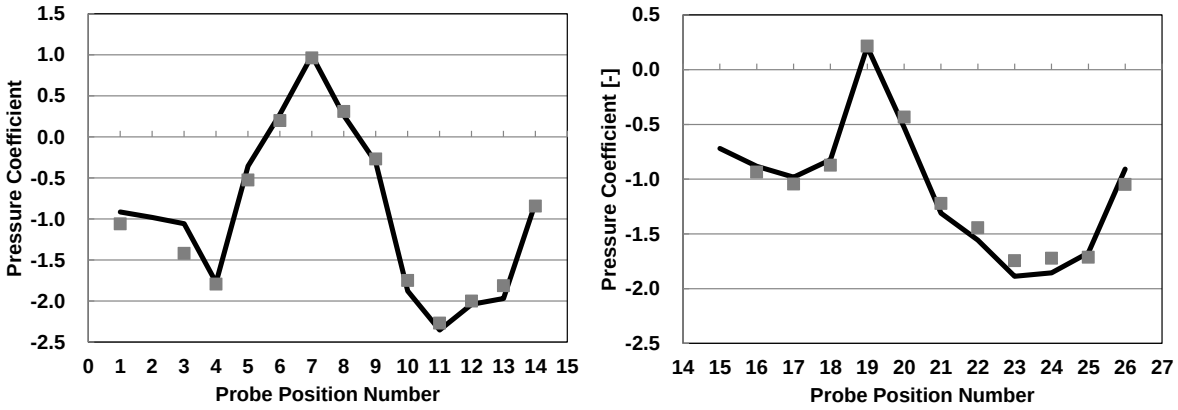

(a) A-plane (b) B-plane

Figure 3. Pressure coefficient. *A-plane of the mirror probe points(left), B-plane of the mirror probe points(right): wall resolved LES, 5.5billion cells* (▬▬) *and experiment* (■).

III. Wall Modeled LES Methodology

A. Solver Formulation

Simulations of the Honda FIT are performed using a low-Mach, isentropic formulation of Cascade's CharLES solver. The solver uses 2nd-order central, conservative operators designed to preserve turbulence dynamics. A low-dissipation scheme is essential for capturing the Reynolds number dependency of the mirror boundary layer as numerical viscosity can alter the flow regime. Accuracy is then managed through wall modeling (section III.B.) and by applying appropriate mesh resolution (section III. C.). Efficient time advancement is obtained through the solver's isentropic formulation and is discussed next.

Incompressible formulations of the Navier-Stokes equations are efficient for the time integration of low Mach number flows by avoiding the time step (or stiffness) associated with the propagation of acoustic waves. The attenuation of all acoustic waves has two immediate consequences. First and most obvious, it is often desirable to compute the acoustic field, even in low speed flows. Second, the incompressible equations are limiting behavior where the speed of sound is infinitely larger than the convective velocity making the governing equations elliptic in nature. This yields a poorly conditioned system of governing equations that are difficult to solve.

We, then, seek a low Mach formulation that preserves a finite speed of sound and admits lower frequency acoustic waves without sacrificing time steps that scale with the convective CFL limit. This is accomplished by approximating the flow as isentropic to yield a coupling between the density and pressure perturbations in a variable density setting. The introduction of a finite sound speed also results in a better conditioned set of governing equations allowing for faster and more scalable solutions. A brief derivation of the formulation is presented below.

1. Low-Mach Governing Equations

We admit a two variable expansion of the density, ρ, of the fluid in terms of its entropy, s, and pressure, p

$$d\rho = \left.\frac{\partial \rho}{\partial s}\right|_p ds + \left.\frac{\partial \rho}{\partial p}\right|_s dp \qquad (1)$$

Assuming the flow is low-Mach, we will admit an approximation that the flow is isentropic. Then integrating Eqn. 1 from a reference state, (s_{ref}, p_{ref}), to another thermodynamic state, (s_{ref}, p) yields (dropping the entropy argument)

$$\rho(p) - \rho_{ref} = \int_{p_{ref}}^{p} c^2 dp = c^2\left(p - p_{ref}\right) \qquad (2)$$

where c is the speed of sound. We can now derive a modified fractional step algorithm from the relationship in Eqn. 2. The continuity and momentum equations for a variable density flow are given by

$$\frac{\partial \rho}{\partial t} + \frac{\partial \rho u_j}{\partial x_j} = 0 \qquad (3)$$

$$\frac{\partial \rho u_i}{\partial t} + \frac{\partial \rho u_i u_j}{\partial x_j} = -\frac{\partial p}{\partial x_i} + \frac{\partial \sigma_{ij}}{\partial x_j} \qquad (4)$$

where σ_{ij} represents the viscous stresses. We assume a fractional step time advancement of Eqns. 3 and 4:

$$A\rho u^* = r^n \qquad (5)$$

$$\rho^{n+1}u^{n+1} - D\rho u^* = -\alpha \Delta t G p \qquad (6)$$

where A, D and G denote the discrete implicit time advancement operator, discrete divergence operator and discrete gradient operator, respectively and α is a coefficient relating to the particular choice of time advance scheme. Taking the discrete divergence of Eqn. 6 and using Eqn. 5 yields

$$-\left.\frac{\partial \rho}{\partial t}\right|^{n+1} - D\rho u^* = -\alpha \Delta t D G p \qquad (7)$$

For simplicity, let us admit the following discretization of the density time derivative in Eqn. 7

$$\left.\frac{\partial \rho}{\partial t}\right|^{n+1} = \frac{\rho^{n+1} + \rho^n}{\Delta t} \qquad (8)$$

We now use Eqn. 2 in the above expression and substitute into Eqn. 7 to yield a Helmholtz system for the pressure

$$-\frac{1}{c\Delta t} p + \alpha \Delta t D G p = D\rho u^* + \frac{\rho_{ref} - \rho^n}{\Delta t} \qquad (9)$$

The time step is completed using the relations in Eqns. 2 and 6 for ρ^{n+1} and u^{n+1}, respectively.

B. Dynamic slip wall modeling

Wall modeling for large-eddy simulation is a necessity in order for calculations to be computationally tractable in high Reynolds number wall bounded flows. Wall resolved LES suffers from a near quadratic increase in the number of grid points with respect to the Reynolds number ($N \sim Re^{13/7}$) as compared with a linear scaling for wall modeled LES[6]. Traditional wall modeling has computed the wall stress by solving thin boundary layer equations or other near-wall RANS equations. These closures rely on a number of assumptions and empirical models: presumed shape of the boundary layer profile, attached flow, no pressure gradient effects, turbulent flow, matching locations, and/or a well-known mixing length controlled by tunable coefficients. While these models have had success in predicting a number of flows (primarily, canonical attached boundary layers although there are applications to more complex flows), the underlying empiricism limits its predictive capability.

The dynamic slip wall modeling framework, instead, derives a wall boundary condition directly from the filtered governing equations. The LES governing equations solve for the dynamics of filtered variables (e.g., velocity):

$$\bar{u}_i(x) = \int G\left(x', x; \Delta\right) u_i\left(x'\right) dx' \qquad (10)$$

A wall boundary condition for the filtered variables is then derived from the filtered governing equations by assuming a specific choice of the filter kernel in Eqn. 10. This approach makes no assumptions about the state of the local boundary layer. The remaining parameter in the wall boundary condition related to the near-wall filter width is computed via a dynamic procedure making this approach free of any a priori specified coefficients. For a full derivation please refer to Bose and Moin[5].

C. Voronoi Diagram based Meshing

Honda FIT computational grids are constructed using a flexible Voronoi diagram based approach developed by Cascade Technologies. Given a set of mesh points distributed at the desired grid density, the Voronoi diagram uniquely defines the cell volumes and mesh connectivity. Put more simply, in a Voronoi diagram each point "owns"

the region of space closer to itself than any other point. A Voronoi mesh is a natural generalization of a hexahedral mesh with localized hanging-node refinement. Figure 4 shows a comparison of such a mesh with a Voronoi diagram based mesh built from the Cartesian mesh nodes.

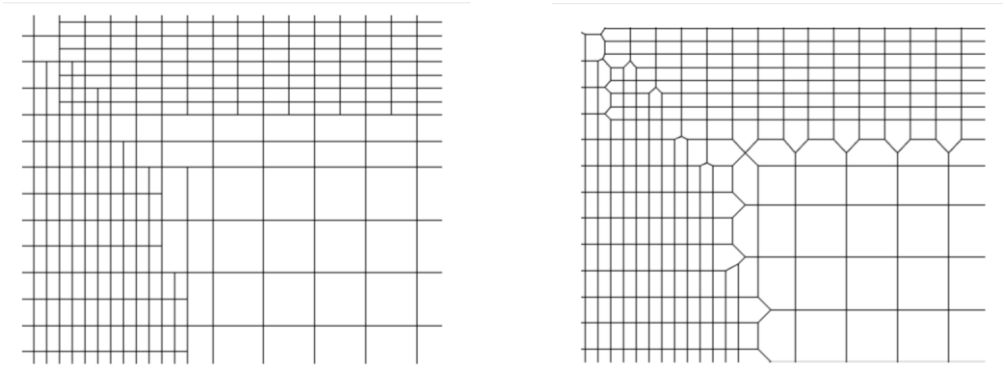

(a) Cartesian Mesh (b) Voronoi Mesh

Figure 4. Mesh Comparison. *Illustration of the close relationship between a Cartesian adapted mesh (a) and a Voronoi mesh generated using the nodes of the adapted Cartesian mesh (b).*

The generation of a three-dimensional Voronoi mesh inside a complex fluid volume is essentially a three step iterative process:

1. Define the generating point set. These are coordinates of the Voronoi vertices that will eventually correspond to the locations of unknowns in the flow solver. A valid Voronoi diagram exists for any set of points, however the spacing and arrangement of these points will control the quality and topology of the resulting mesh,
2. Generate the Voronoi diagram, in parallel, from the generating point set.
3. If the mesh is not sufficiently accurate, or smooth, either enrich or smooth the locations of the generating point set, and repeat step 2.

An extremely powerful aspect of using Voronoi diagrams to produce computational meshes is that the definition of the Voronoi site locations uniquely describes the Voronoi mesh, including all geometric information (e.g. volumes, face normals and areas), and connectivity (e.g. nearest neighbors). This deterministic connection between the point locations and the resulting mesh dramatically simplifies the methodologies employed for mesh adaptation and manipulation.

One import mesh manipulation in the context of LES is smoothing. Rapid grid transitions and highly skewed cells can distort the turbulent structures being transported. Smoothing a Voronoi mesh reduces to smoothing a distribution of points, free from the headaches of its impact on mesh connectivity. The Honda FIT grids use a smoothing algorithm called Lloyd iteration. Lloyd iteration makes use of the fact that the Voronoi points and the centroids of the resulting Voronoi cells are not necessarily coincident. When they are, the Voronoi mesh is called centroidal. In the most basic implementation of Lloyd iteration, the generating points are moved to the centroids of their Voronoi cells, and the Voronoi mesh is recomputed (Figure 5).

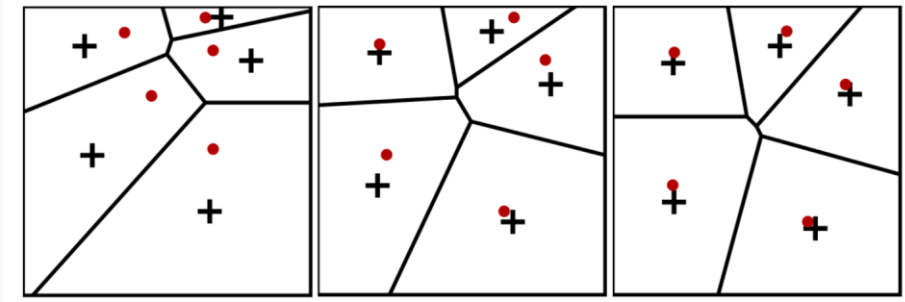

Figure 5. Mesh Smoothing. *Illustration of 2 Lloyd iterations, where the Voronoi points (red) are moved to the Voronoi cell centroids (black +) and the Voronoi diagram is recomputed. Note how the mesh becomes more uniform and centroidal.*

IV. Full-Vehicle Results

A. Numerical setup

For consistency with the wall-resolved LES, a super-critical Reynolds number case (U_∞ = 100km/h) is used for initial evaluations of the effectiveness of the wall modeled approach. Figure 6. shows the calculation domain and Voronoi mesh. The computational domain ranges from -25m to 50m in the x direction, from -15m to 15m in the y direction, and from 0m to 15m in the z direction. Porous media modeling was applied in the radiator and condenser zones using empirical coefficients. The tires and wheels are in a stationary condition. The inflow velocity is 100km/h with no perturbations. A non-reflecting outflow boundary condition is applied to allow pressure fluctuations to exit the domain. The sub-grid scale turbulence model is the Vreman model[11].

Generally, the resolution required to resolve the turbulent boundary-layer is estimated as normalized wall distance y^+. In particular, several nodes are necessary in the viscous bottom layer (y+ less than 5) as a condition for a non-slip wall. Wall modeling relaxes the resolution requirements in the wall normal direction allowing for reductions in computational cost. Meshes were produced using the Voronoi approach with 20 Lloyd iterations to smooth grid transitions as discussed in Section IIIC. The initial generating point set was modified iteratively as the appropriate resolution for the wall-modeled simulations was sought. Table 2 contains a summary of the different simulation approaches and meshes used in the present work. Compared to the WRLES from Reference 9, there is a large mesh size reduction for the present simulation which comes from a combination of two factors: (1) relying on the wall model to capture the smallest near wall scales and (2) focusing mesh refinement only on the mirror region. In this paradigm, the full vehicle geometry is used to condition the flow, though all vehicle boundary layers are not resolved. For example, Figure 7 shows time-averaged simulation result for the baseline case LES1 without wall modeling. Qualitatively, the result shows the typical flow features around a compact vehicle (e.g. a large wake region, underbody acceleration, etc.) and there is no unphysical oscillation around cell transition regions.

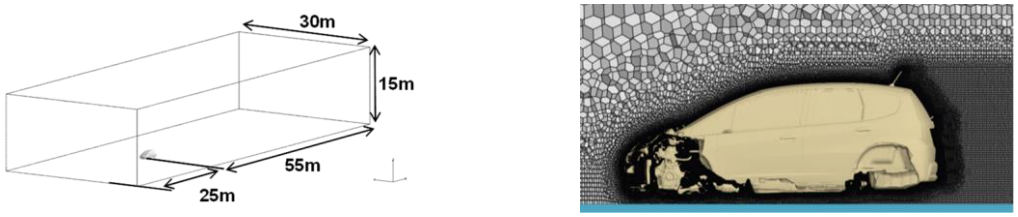

(a) Simulation domain (b) Baseline Voronoi Vehicle Mesh

Figure 6. Simulation conditions. *Domain dimensions and the baseline vehicle mesh remained constant over all computations.*

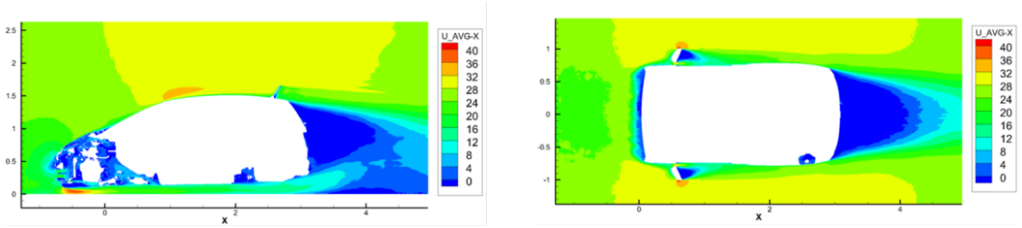

(a) Y=0m plane (b) Z=0.987m plane

Figure 7. Mean Streamwise velocity for LES1.

B. Simulation parameters and methodology

Table 2 summarizes the simulations performed for the present work and compares them to the wall-resolved computation from Reference 9. Mirror wall-normal resolution is listed however it is important to note that the current runs utilized roughly isotropic grid spacing while the cells from WRLES had an aspect ratio of approximately 13. The finest wall normal spacing used in the present simulations was approximately 8 times larger than that used in WRLES.

Case LES1 utilized the baseline mesh shown in Figure 6b. Subsequent mesh modifications built upon the base case by adding refinement near the mirror surface and upstream next to the A-pillar. Figure 8 shows an illustration of mesh refinement in these regions. Figure 9 illustrates the domain regions (A, B, C and the A-pillar) where varied resolution was applied over the runs described in Table 2. The underlying strategy behind mesh generation moving down the rows of Table 2 was to first condition the mirror incident flow with a baseline mesh (LES1). Next, the near-mirror mesh was refined to predict Cp as effectively as possible given the incident flow (WMLES1 and WMLES2). The region upstream of the mirror was then refined in WMLES3 and maintained in WMLES4 to better capture shedding off the A-pillar. Lastly, in WMLES4 an additional patch of refinement was applied to the underside of the mirror (region C) where thin transitional boundary layers are expected.

The wall-modeled surfaces in the domain were also varied over the runs performed in conjunction with the meshing strategy. After the baseline LES1 case, initially only the mirror surface was modeled for WMLES1 and WMLES2. Moving to WMLES3 and WMLES4 wall modeling was applied to the full vehicle. As will be shown, WMLES4 is the most accurate result and LES2 was computed on an identical mesh with wall modeling off to isolate the model's impact.

Case name	Cell count	**Mirror Normal Resolution [mm] (y+)**			A-pillar resolution [mm]	Wall model	Time step [sec]
		A	B	C			
WRLES	**5.5 billion**	**0.015 (0.8)**	**0.015 (0.8)**	**0.015 (0.8)**	**1.0**	**OFF**	**1.0×10^{-6}**
LES1	32.8 million	0.500 **(28)**	0.500 **(28)**	0.500 **(28)**	4.0	OFF	5.0×10^{-5}
WMLES1	35.2 million	0.500 **(28)**	0.250 **(14)**	0.500 **(28)**	4.0	Mirror only	5.0×10^{-5}
WMLES2	51.9 million	0.250 **(14)**	0.250 **(14)**	0.250 **(14)**	4.0	Mirror only	5.0×10^{-5}
WMLES3	53.0 million	0.250 **(14)**	0.250 **(14)**	0.250 **(14)**	0.5	Full vehicle	2.5×10^{-6}
WMLES4	59.4 million	0.250 **(14)**	0.250 **(14)**	0.125 **(6.9)**	0.5	Full vehicle	2.5×10^{-6}
LES2	59.4 million	0.250 **(14)**	0.250 **(14)**	0.125 **(6.9)**	0.5	OFF	2.5×10^{-6}

Table 2. Simulation parameters. *WRLES refers to the result data of Reference 9. Mirror resolution is noted for the three lettered regions identified in Figure 9.*

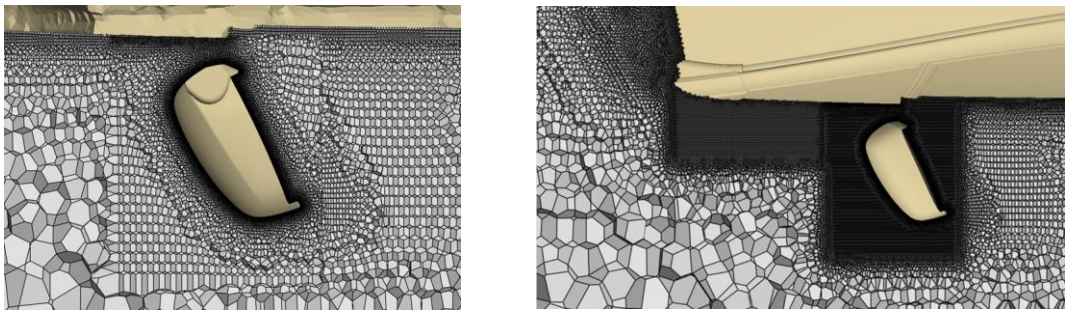

(a) Mirror surface refinement (WMLES1) (b) Upstream A-pillar mesh refinement (WMLES3)

Figure 8. Examples of Voronoi mesh topology for slip wall-modeled LES.

(a) Side mirror refinement regions (b) A-pillar refinement region

Figure 9. Targeted refinement regions on the mirror surface (A, B, and C) and upstream volume adjacent to the A-pillar (red box).

C. Simulation results

The comparison of the Cp distribution between wall resolved and wall modeled LES are shown in Figure 10. The pressure tap positions are in accordance with the Figure 1. The results of the wall resolved LES and experimental Cp are included for reference.

Results from LES1 (without wall modeling), underestimate the pressure at points 22 and 23 while overestimating it near points 10-14, 24, and 25. Sensitivity to the boundary layer treatment was expected in these areas as flow transition was observed in the experimental measurements. WMLES1 improved the Cp distribution near points 10-14, and also 22-23. While improvement near the former set of probes was due in part to additional mesh resolution in region B (see Figure 9a), improvement near 22-23 can be attributed to activation of wall modeling of the mirror surface. WMLES2 attempted to address Cp discrepancies at 4, 24 and 25 from WMLES1. The resolution in region B was applied to the full side mirror in WMLES2. This improved Cp at locations 24 and 25 while it was noted the stagnation point 7 continued to be under predicted. This was hypothesized to be due to an inaccurate representation of the incident flow shed by the upstream A-pillar. WMLES3 added resolution upstream of the mirror and wall modeling on the entire vehicle which shifted the stagnation Cp prediction closer to the experimental measurement. Improvement was also noted in the portions of the horizontal Cp profile closest to the vehicle door (locations 1-4) that were most impacted by flow structure developing around the A-pillar. Unfortunately, the prediction of Cp on the underside of the mirror at point 23 became worse moving from WMLES2 to WMLES3. WMLES4 therefore revisited adding additional mirror resolution, this time in region C as noted in Figure 9a. While the Cp agreement between experiment and WMLES4 at point 23 was not as close as from the wall-resolved simulation, qualitatively the profile from 23 to 24 became flatter as seen in the reference results. With a normalized wall distance, y+, of approximately 7.0, WMLES4 yielded its prediction of the Cp curve without a grid point formally in the viscous bottom layer.

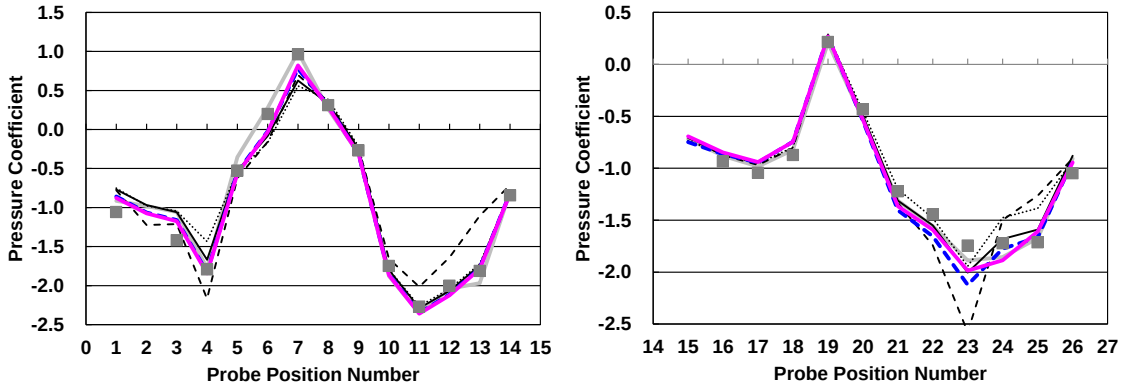

(a) A-plane (b) B-plane

Figure 10. Cp comparison between WRLES and WMLES on the inflow condition of 100km/h. *A-plane of the mirror probe points(left), B-plane of the mirror probe points(right): WRLES* ( ), *LES1* ( ), *WMLES1* ( ), *WMLES2* ( ), *WMLES3* ( ), *WMLES4* ( ) *and experiment* ( ).

D. Impact of Wall Modeling

To clarify the impact of the wall model in WMLES4, LES2 was computed on an identical grid with wall modeling off (i.e. no-slip boundary conditions were utilized). Figure 11 shows a comparison of these cases with the reference data. In LES2 the Cp distribution was underestimated in similar fashion to the coarser computations. Figure 12 shows contours of mean streamwise velocity on the underside of the mirror near points 22 through 26. WMLES4, LES2 as well as the fully resolved flow are shown. Reversed flow highlighting the separated region is blue in color. The reattachment distance of the dynamic slip wall modeled case (b) is similar to the wall resolved case (a). By contrast, not applying wall modeling (c) resulted in a smaller separation. These results show that the wall model not only improves the Cp distribution on the surface but also the flow field.

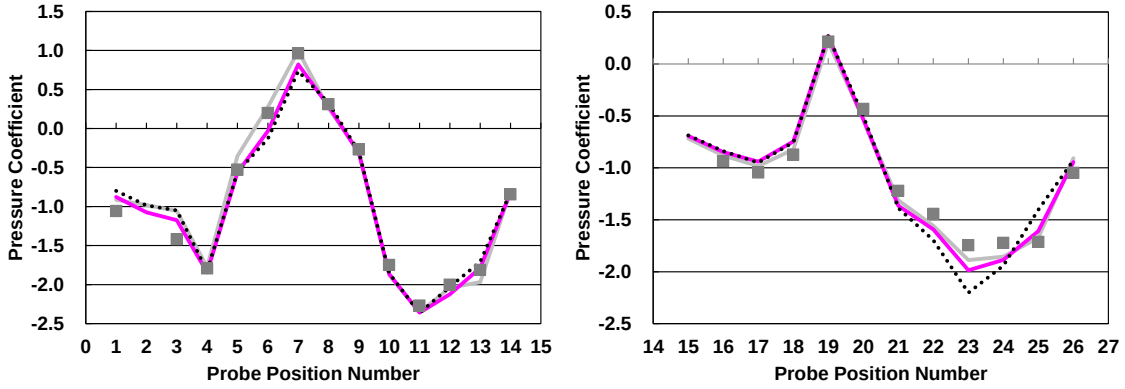

(a) A-plane (b) B-plane

Figure 11. The influence of the wall model on the inflow condition of 100km/h. *A-plane of the mirror probe points(left), B-plane of the mirror probe points(right): WRLES* ( ), *WMLES4* ( ), *LES2* ( ) *and experiment* ( ).

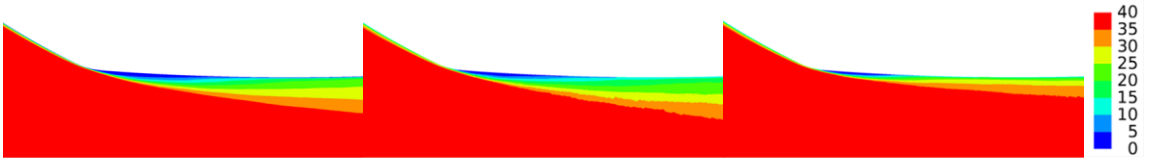

(a) WRLES (b) WMLES4 (c) LES2

Figure 12. Flow field of the streamwise mean velocity around pressure tap point 22 to 26. *The section is the B-plane of the mirror, wall resolved LES(WRLES) (left) , wall modeled LES(WMLES4)(center), without wall model(LES2)(right).*

E. Calculation cost

The calculation cost of each case is shown in Table 4. The calculation time for the gathering of statistics is approximately 9 mirror flow-through times based on a mirror length of 0.15m and the free stream velocity. Note that the wall-resolved and wall-modeled simulations were performed on different systems. It is clear that the use of wall modeling leads to a significant reduction in total calculation cost. For rigorous comparison of the solver performance, the normalized cost is presented in core-hours per million cells per step and it can be seen that wall modeling added only a modest additional cost to solver performance. Given the additional efficiencies in meshing and time step size, this type of full vehicle LES has been practical for industrial applications

Case name	Software	Calculation core	Total calculation cost, core×h	Normalized calculation cost, core×h/Millions cell/step
WRLES	**FVM code**[7,8]	**36,864**	**3,300,424**	**0.012**
WMLES4	CharLES	1,024	16,047	0.013

Table 4. Calculation costs. *bold font indicate the result data of Reference9.*

V. Conclusion

This investigation illustrated that the dynamic slip wall model and Voronoi meshing methodologies which were implemented in CharLES could predict boundary layer separation from a vehicle side mirror at a super-critical Reynolds number. Accurately capturing the Cp distribution on the side mirror required precise management of the interplay between mesh resolution and wall modeling. Even with slip wall modeling, the presence of thin, laminar boundary layers imposed significant resolution requirements on the underlying mesh. The minimum normalized wall distance, y+, of the final wall modeled case (WMLES4) was approximately 7.0, however, indicating the potential to relax the resolution from that of a formally wall resolved grid. In particular, wall normal resolution of the finest wall modeled case was 8 times larger than that of the wall resolved LES. Given the wall model formulation did not dramatically increase the normalized solver cost and the Voronoi meshing approached allowed targeted refinement, the number of core-hours required for such an LES is dramatically less. With such a reduction LES becomes a viable option for industrial use.

Acknowledgments

Wall resolved large eddy simulation used computational resources of the “K computer” provided by the RIKEN Advanced Institute for Computational Science through the HPCI System Research project (Project ID:hp140011)

References

[1] Powell, A., “Theory of vortex sound,” *Journal of the Acoustical Society of America*, 36, pp.177-195, 1964.

[2] Nouzawa, T., Li, Y., Kasaki, N., and Nakamura, T., “Mechanism of Aerodynamic Noise Generated from Front-Pillar and Door Mirror of Automobile,’’ *J. Environment Eng.*, Vol. 6(3) :615-626, 2011, doi:10.1299/jee.6.615.

[3] Hamamoto, N., Okutsu, Y., and Yanagimoto, K., “Investigation for the Effect of the External Noise Sources onto the Interior Aerodynamic Noise,” *SAE Int.*, 2013-01-1257, 2013, doi:10.4271/2013-01-1257.

[4] Ambo, K., Morishita, K., Yoshino, T., and Teramura, M., "Identification of Mechanism of Transmission of Flow-induced Noise through Glass for Vehicle Interior Noise Reduction," *Honda R&D Technical Review*, 25(2), 2013.

[5] Bose, S., and Moin, P., "A dynamic slip boundary condition for wall-modeled large-eddy simulation," *Physics of Fluids*, 26, 015104, 2014.

[6] Choi, H., and Moin, P., "Grid-point requirements for large eddy simulation: Chapman's estimates revisited," *Physics of Fluids*, 24:011702, 2012.

[7] Tsubokura, M., Nakashima, T., Kitoh, K., Sasaki, Y. et al., "Development of an Unsteady Aerodynamic Simulator Using Large-Eddy Simulation Based on High-Performance Computing Technique," *SAE Int. J. Passeng. Cars – Mech. Syst.* 2(1):168-178, 2009, doi:10.4271/2009-01-0007.

[8] Onishi, K., Tsubokura, M., "Optimized preprocessing of tens of billions of grids in a full-vehicle aerodynamic simulation on the K-computer," *International Vehicle Aerodynamics Conference 2014*, C1385 008, pp.149-158, 2014.

[9] Ambo, K., Yoshino, T., and Teramura, M., "Wall-Resolved LES to predict the boundary-layer separation around the side-mirror of a full-scale vehicle at the critical Reynolds number," *International Vehicle Aerodynamics Conference 2016*, pp.127-139, 2016.

[10] Spalding, D. B., "A Single Formula for the "Law of the Wall," *Journal of Applied Mechanics*, vol.28(3), pp.455-458, 1961, doi:10.1115/1.3641728.

[11] Vreman, A., "An eddy-viscosity subgrid-scale model for turbulent shear flow: Algebraic theory and applications," *Physics of Fluids*, Vol. 16, Jan 2004, pp. 3570.